Cubic $AgPb_mSbTe_{2+m}$: Bulk Thermoelectric Materials with High Figure of Merit

Kuei Fang Hsu *et al.*

Science **303**, 818 (2004);
DOI: 10.1126/science.1092963

Science (print ISSN 0036-8075; online ISSN 1095-9203) is published weekly, except the last week in December, by the American Association for the Advancement of Science, 1200 New York Avenue NW, Washington, DC 20005.

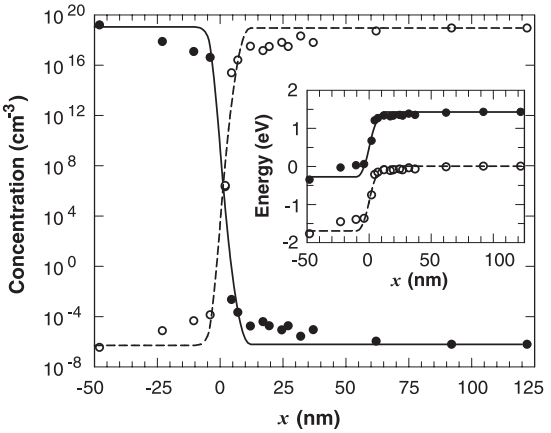

Fig. 4. Carrier profile across the *p-n* junction shown in Fig. 2. Solid and dashed lines are electron and hole concentrations, respectively, calculated from the SIMS dopant profile. Solid and open circles are electron and hole concentrations, respectively, calculated from the SThEM results. Inset: Energy diagram of the *p-n* junction. Solid and open circles are the conduction and valence band edge, respectively, calculated from the SThEM results. Solid and dashed lines are calculated from the SIMS dopant profile.

agreement, although the match is poor at the edges of the depletion region (likely as a result of the continuum assumption and the depletion approximation invoked for the calculation based on SIMS). An important feature is the ability of SThEM to resolve the location of the electronic junction to within 2 nm. This position corresponds to the location where the majority carrier type changes, resulting in the abrupt sign change of the thermoelectric voltage. Because there is no external electrical bias across the tip-sample junction, the SThEM measurement does not suffer the severe tip voltage–induced band-bending effect that exists in STM or scanning capacitance microscopy, where a very large external electric field ($\sim 10^9$ V/m) exists at the tip-sample gap and shifts the junction location. The resolution shown here for junction delineation shows a significant improvement over most of the characterization techniques available today.

References and Notes

1. G. Mahan, B. Sales, J. Sharp, *Phys. Today* **50**, 42 (1997).
2. F. J. DiSalvo, *Science* **285**, 703 (1999).
3. H. Edwards, Q. Niu, A. de Lozanne, in *Wiley Encyclopedia of Electrical and Electronics Engineering*, J. G. Webster, Ed. (Wiley, New York, 1999), vol. 22, pp. 80–90.
4. L. D. Hicks, M. S. Dresselhaus, *Phys. Rev. B* **47**, 12727 (1993).
5. L. D. Hicks, M. S. Dresselhaus, *Phys. Rev. B* **47**, 16631 (1993).
6. R. Venhatasubramanian, E. Siivola, T. Colpitts, B. O'Quinn, *Nature* **413**, 597 (2001).
7. T. C. Harman, P. J. Taylor, M. P. Walsh, B. E. LaForge, *Science* **297**, 2229 (2002).
8. P. de Wolf, R. Stephenson, T. Trenkler, T. Hantschel, W. Vandervorst, *J. Vac. Sci. Technol. B* **18**, 361 (2000).
9. C. C. Williams, H. K. Wickramasinghe, *Nature* **344**, 317 (1990).
10. J. C. Poler, R. M. Zimmermann, E. C. Cox, *Langmuir* **11**, 2689 (1995).
11. See supporting data on *Science* Online.
12. A. Vaterlaus, R. M. Feenstra, P. D. Kirchner, J. M. Woodall, G. D. Pettit, *J. Vac. Sci. Technol. B* **11**, 1502 (1993).
13. A. R. Smith *et al.*, *J. Vac. Sci. Technol. B* **12**, 2610 (1994).
14. N. D. Jäger *et al.*, *Phys. Rev. B* **67**, 165307 (2003).
15. K. P. Pipe, R. J. Ram, A. Shakouri, *Phys. Rev. B* **66**, 125316 (2002).
16. J. F. Bresse, A. C. Papadopoulo, *J. Appl. Phys.* **64**, 98 (1988).
17. G. D. J. Smit, S. Rogge, T. M. Klapwilk, *Appl. Phys. Lett.* **81**, 3852 (2002).
18. For a planar junction, the depletion width (W) is related to the barrier height (φ) as $W = (2\varphi\varepsilon_s/e^2N)^{1/2}$, where ε_s is the dielectric constant and N is the doping density. For a point contact of a hemispherical contact area with a radius of a_o, we obtain the radius of hemispherical depletion zone as $r_o \approx (3a_o\varepsilon_s\varphi/e^2N)^{1/3}$, provided that $a_o \ll r_o$. Using $a_o = 1$ nm, $\varphi = 0.5$ eV, and $N = 10^{19}$/cm^3, we find that $r_o \sim 5$ nm. Note that in the derivation we assume a uniform and continuous charge distribution. However, r_o is now very close to the average interdopant spacing, and one expects that this assumption breaks down. Nonetheless, on the basis of the qualitative scaling behavior, one can still conclude that $r_o < W$.
19. R. Trzcinski, E. Gmelin, H. J. Queisser, *Phys. Rev. Lett.* **56**, 1086 (1986).
20. O. I. Shklyareskii, A. G. M. Jansen, J. G. H. Hermsen, P. Wyder, *Phys. Rev. Lett.* **57**, 1374 (1986).
21. L. Weber, M. Lehr, E. Gmelin, *Phys. Rev. B* **46**, 9511 (1992).

22. Supported by NSF grants DMR-0210383, DMR-0306239, and CTS-0239179 and by the Texas Advanced Technology Program. L.S. thanks U. Ghoshal for helpful discussions on SThEM.

Supporting Online Material

www.sciencemag.org/cgi/content/full/303/5659/816/DC1
Materials and Methods
References

17 September 2003; accepted 11 December 2003

Cubic $AgPb_mSbTe_{2+m}$: Bulk Thermoelectric Materials with High Figure of Merit

Kuei Fang Hsu,[1] Sim Loo,[2] Fu Guo,[2] Wei Chen,[3] Jeffrey S. Dyck,[3] Ctirad Uher,[3] Tim Hogan,[2] E. K. Polychroniadis,[4] Mercouri G. Kanatzidis[1]*

The conversion of heat to electricity by thermoelectric devices may play a key role in the future for energy production and utilization. However, in order to meet that role, more efficient thermoelectric materials are needed that are suitable for high-temperature applications. We show that the material system $AgPb_mSbTe_{2+m}$ may be suitable for this purpose. With $m = 10$ and 18 and doped appropriately, *n*-type semiconductors can be produced that exhibit a high thermoelectric figure of merit material ZT_{max} of ~2.2 at 800 kelvin. In the temperature range 600 to 900 kelvin, the $AgPb_mSbTe_{2+m}$ material is expected to outperform all reported bulk thermoelectrics, thereby earmarking it as a material system for potential use in efficient thermoelectric power generation from heat sources.

Thermoelectric devices are generally based on heavily doped semiconductors and can be used for cooling applications or for electricity generation directly from a heat source. When supplied by a temperature differential, thermoelectric semiconductors respond by virtue of the Seebeck effect to produce a voltage that could be used to drive an external load. A broad search has been under way to identify new materials with enhanced thermoelectric properties. Although the emphasis has been on finding materials that are superior to the well-known $Bi_{2-x}Sb_xTe_{3-y}Se_y$ alloys used in cooling, interest in developing materials with high ZT values (*1*) at high temperatures for direct energy conversion has been increasing. Several classes of materials are currently under investigation, including complex chalcogenides (*2*), skutterudites (*3*, *4*), half-Heusler alloys (*5*), metal oxides (*6*), intermetallic clathrates (*7*–*9*), and pentatellurides (*10*). In addition, artificial superlattice thin-film structures grown from chemical vapor deposition, such as Bi_2Te_3/Sb_2Te_3 (*11*), and by molecular beam epitaxy (MBE), such as $PbSe_{0.98}Te_{0.02}$/PbTe (*12*, *13*), have been introduced with substantially enhanced ZT values relative to those of their bulk counterparts. Marking an important development in this area, specially constructed Bi_2Te_3/Sb_2Te_3 superlattices were reported to exhibit a very high ZT of ~2.4 at room temperature (*14*). The MBE-grown thin-film $PbSe_{0.98}Te_{0.02}$/PbTe systems (*11*, *12*) feature peculiar pyramidal-shaped "nanodots" of PbSe that form spon-

taneously (surrounded by the higher band gap matrix material PbTe). The resulting samples possess a *ZT* of ~2 at elevated temperatures (about 500 to 700 K) (*15*). Nevertheless, because the vast majority of applications require materials in large quantities, it would therefore be desirable to have compositions that could generate similar *ZT* values in a bulk material.

Our approach in developing high-performance bulk thermoelectric materials has focused on compounds with low-dimensional structures to take advantage of the large anisotropy in carrier effective masses associated with such systems. Along these lines, $CsBi_4Te_6$ has been identified as a material showing a *ZT* of 0.8 at 225 K (*16*), which is 40% greater than that of the $Bi_{2-x}Sb_xTe_{3-y}Se_y$ alloys. We report on a family of bulk cubic compounds with complex composition and general formula $Ag_nPb_mM_nTe_{m+2n}$ (M = Sb,Bi), which combine a set of desirable features, e.g., isotropic morphology, high crystal symmetry, low thermal conductivity, and ability to control the carrier concentration. We demonstrate that members of this family can be optimized to produce high *ZT* values (~2) at elevated temperatures.

The $Ag_nPb_mSb_nTe_{m+2n}$ compounds possess an average NaCl structure ($Fm\bar{3}m$ symmetry); the metals Ag, Pb, and Bi are disordered in the structure on the Na sites, whereas the chalcogen atoms occupy the Cl sites (Fig. 1A). The formula is charge-balanced because the average charge on the metal ions is 2+ and on the chalcogen ions it is 2−. The $Ag_nPb_mBi_nTe_{m+2n}$ formulation can generate a large number of compositions by "dialing" *m* and *n*, allowing considerable potential for property control. We find that several members of this family are capable of achieving higher power factors and high *ZT* values at high temperatures suitable for high-efficiency heat–to–electrical energy conversion applications. A series of $AgPb_mSbTe_{2+m}$ ($n = 1$) samples were prepared in which the lattice parameters vary smoothly with *m*. The x-ray diffraction pattern and unit cell parameter variation for several members of the series are shown (Fig. 1, B and C).

Ingots with the composition $AgPb_{10}SbTe_{12}$ (*17*) show an electrical conductivity of >520 S/cm and thermopower (i.e., Seebeck coefficient) of −154 μV/K at room temperature, resulting in a power factor of 12.3 μW/cm·K^2. This value is larger than that of other candidate materials like $K_2Bi_8Se_{13}$, which has a power factor of 10.0 μW/cm·K^2 (*18*). A further enhancement in the power factor is observed when we depart from the ideal stoichiometry $Ag_{1-x}Pb_{10}Sb(Bi)Te_{12}$, with a room-temperature value of 17.0 μW/cm·K^2. This enhancement is achieved mainly through an increase in conductivity to 740 S/cm without a noticeable loss in the Seebeck coefficient. From the temperature dependence of electrical conductivity and thermopower of such a sample over a wide temperature range (Fig. 2A), the conductivity decreases with rising temperature, consistent with a degenerate semiconductor. At 700 K, the electrical conductivity is 135 S/cm and the thermopower −290 μV/K, giving a power factor of 11.4 μW/cm·K^2. Thermal conductivity measurements for bulk $Ag_{1-x}Pb_{10}Sb(Bi)Te_{12}$ (Fig. 2B) revealed a low value of 1.30 W/m·K at 300 K. This is lower than that of bulk PbTe and comparable to that of Bi_2Te_3. The thermal conductivity above 300 K was obtained with a different experimental method (flash diffusivity/specific heat) (*19*). We obtained the *ZT* dependence on temperature and found that it reaches 1 at 700 K (Fig. 2C). Given the rising trend, we expect an even higher value (~1.3) at 900 K.

When $n = 1$ and $m = 18$, the composition is $AgPb_{18}SbTe_{20}$. These samples also possess an average cubic $Fm\bar{3}m$ symmetry and an optical band gap of 0.26 eV (fig. S1). Again, here the properties of $AgPb_{18}SbTe_{20}$ are promising but not exceptional, yet a departure from stoichiometry to give $Ag_{1-x}Pb_{18}SbTe_{20}$ results in a large jump in the power factor to impart a high

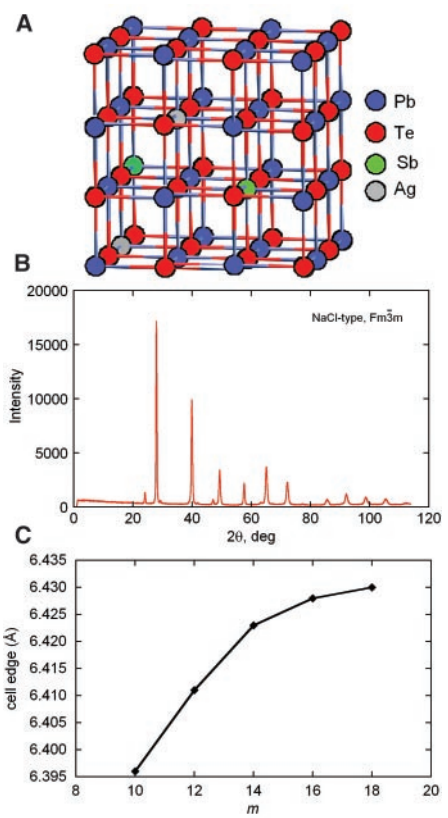

Fig. 1. (**A**) Average ideal $Fm\bar{3}m$ crystal structure of $AgPb_mMTe_{2+m}$ (M = Sb, Bi) series. (**B**) X-ray diffraction pattern (Cu Kα radiation) of $AgPb_{10}SbTe_{12}$. (**C**) Lattice parameter variation of $AgPb_mSbTe_{2+m}$ as a function of *m*. The elemental formulae reported in the paper are nominal, but they have been confirmed with microprobe energy-dispersive spectroscopic analysis.

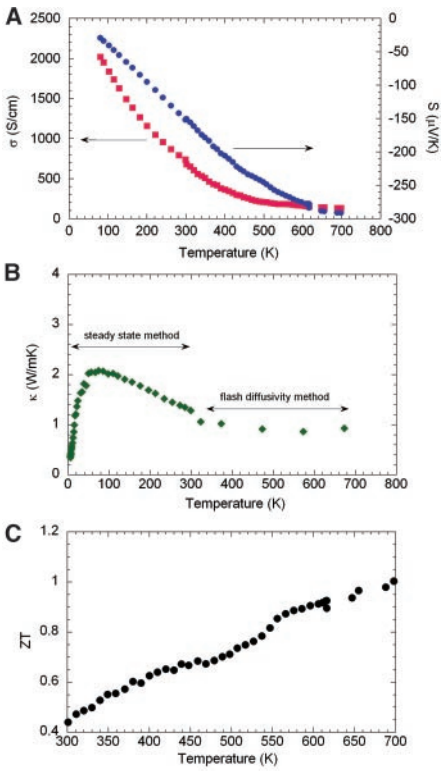

Fig. 2. Variable-temperature charge transport and thermal transport data for $AgPb_{10}SbTe_{12}$: (**A**) Electrical conductivity (σ) and thermopower (*S*). (**B**) Total thermal conductivity (κ) in the range 6 to 700 K. (**C**) *ZT* as a function of temperature. Thermal conductivity and Seebeck coefficient were determined with a longitudinal steady-state method over the temperature range 4 to 300 K. Samples were attached (using either a low–melting point solder or silver-loaded epoxy) to the cold tip of the cryostat, while the other end of the sample was provided with a small strain-gauge resistor (thin film), which serves as a heater. The temperature difference across the sample was measured with a differential Chromel-Constantan thermocouple. All three measurements were made simultaneously in the same sample. The samples were cut in about 3 mm by 3 mm by 5 mm dimensions. There was inevitable radiation loss during the thermal conductivity measurements at high temperatures, and therefore the data were corrected based on the T^3 law (*24*). The Seebeck voltage was measured with thin copper wire, the thermopower of which was calibrated against a high-*TC* superconductor up to 134 K. The uncertainty in the electrical conductivity and Seebeck measurements is better than ±4%, whereas for the total thermal conductivity it is less than ±10%. In the region 300 to 800 K, the electrical conductivity and thermoelectric power data were collected in a high-temperature measurement system (*25*).

[1]Department of Chemistry, [2]Electrical and Computer Engineering and Materials Science and Mechanics, Michigan State University, East Lansing, MI 48824, USA. [3]Department of Physics, University of Michigan, Ann Arbor, MI 48109, USA. [4]Physics Department, Aristotle University of Thessaloniki, 54124 Thessaloniki, Greece.

*To whom correspondence should be addressed. E-mail: kanatzid@cem.msu.edu

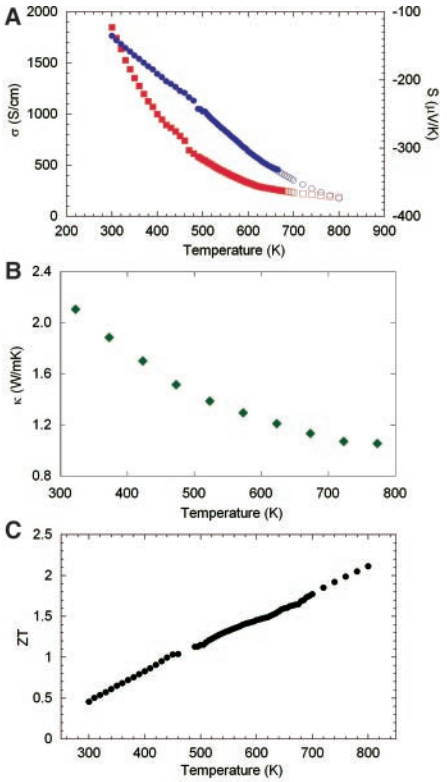

Fig. 3. Variable-temperature charge transport and thermal transport data for $AgPb_{18}SbTe_{20}$: (**A**) Electrical conductivity (σ) and thermopower (*S*). (**B**) Total thermal conductivity (κ) in the range 300 to 800 K. The data were obtained as described in (*19*). (**C**) Thermoelectric figure of merit, *ZT*, as a function of temperature.

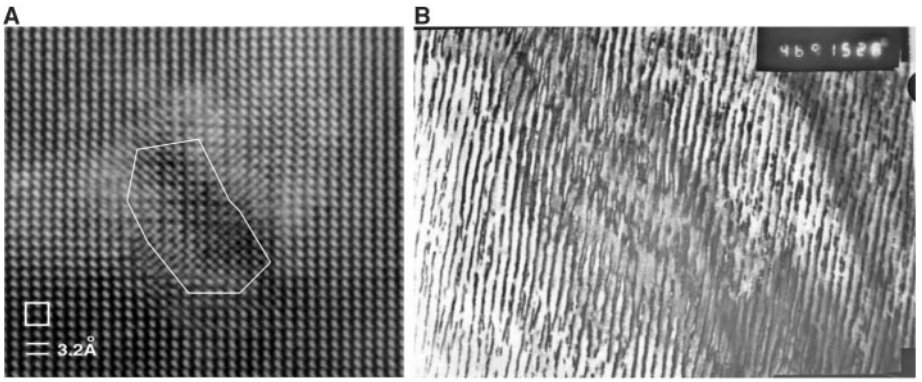

Fig. 4. (**A**) TEM image of a $AgPb_{18}SbTe_{20}$ sample showing a nano-sized region (a "nanodot" shown in the enclosed area) of the crystal structure that is Ag-Sb–rich in composition. The surrounding structure, which is epitaxially related to this feature, is Ag-Sb–poor in composition with a unit cell parameter of 6.44 Å, close to that of PbTe. (**B**) Compositional modulations over an extended region of a $AgPb_{10}SbTe_{12}$ specimen. The spacing between the bands is ~20 to 30 nm. In essence, the observed compositional modulation is conceptually akin to the one found in the artificial PbSe/PbTe superlattices (*15*). In the latter, the compositional modulation exists at least along the stacking direction.

ZT value to this material. The $m = 18$ samples have generally higher electrical conductivity; optimized systems reach ~1850 S/cm at room temperature and a thermopower of −135 μV/K (Fig. 3A) (*20*). The negative value indicates an *n*-type semiconductor. When the temperature rises, the conductivity drops smoothly, as expected for a degenerate semiconductor, whereas the thermopower rises steadily in nearly a straight line, reaching −335 μV/K at 700 K and a power factor of 28.0 μW/cm·K^2. The power factor observed at 700 K is one of the highest among known materials and matches those observed in the PbTe/PbSe superlattices (*12*, *15*). The total thermal conductivity of $Ag_{1-x}Pb_{18}SbTe_{20}$ is shown over a wide temperature range (Fig. 3B) and is ~2.3 W/m·K at room temperature (*19*). The *ZT* of $Ag_{1-x}Pb_{18}SbTe_{20}$ calculated with experimental σ and *S* data measured from 300 to 800 K, and with κ data measured from 300 to 800 K, reaches a value of 2.1 at 800 K (Fig. 3C).

To what can we attribute the enhanced thermoelectric properties of $AgPb_mSbTe_{m+2}$ systems? The answer may lie in the nature of the microstructure of these materials at the nanoscopic level. One explanation could be the presence of quantum "nanodots" in these materials, similar to those found in the PbSe/PbTe MBE–grown thin films. The $Ag_nPb_mSb_nTe_{m+2n}$ materials are derived by isoelectronic substitution of Pb^{2+} ions for Ag^+ and Sb^{3+} (or Bi) in the lattice. This generates local distortions, both structural and electronic, that are critical in determining the properties of $Ag_nPb_mSb_nTe_{m+2n}$. For example, at issue is how the Ag^+ and Sb^{3+} ions are distributed in the structure, i.e., homogeneously or inhomogeneously. Arguably, one might expect an inhomogeneous distribution given the different formal charges of +1/+3 versus +2 arising from Coulombic interactions. A completely homogeneous Ag^+ and Sb^{3+} dispersion in the $Fm\bar{3}m$ lattice would require the complete separation of the Ag^+ and Sb^{3+} pair over long distances, which could create charge imbalances in the vicinity of these atoms. Therefore, barring any compensation effects from the Te sublattice, electroneutrality reasons alone require that Ag^+ and Sb^{3+} ions be generally found near one another (<5 to 6 Å). Given the relatively high concentrations of Ag^+-Sb^{3+} in the $AgPb_{18}SbTe_{20}$ (<10 mol%), these essentially Coulombic factors could act to favor compositional modulations in the crystal that arise from regions of high Ag/Sb and high Pb concentration. Preliminary evidence for this comes from high-resolution transmission electron microscopy (TEM) images that indicate inhomogeneities in the microstructure of these materials, showing nanocrystals of a Ag-Sb–rich phase embedded in a PbTe matrix (Fig. 4). A very small region of the sample is indeed Ag-Sb–rich and is surrounded by a PbTe-rich matrix. In other specimens, such as $AgPb_{10}SbTe_{12}$, different compositional modulations were observed that changed in size and shape under different preparation conditions. More detailed TEM studies as well as band structure and Monte Carlo Coulomb calculations in the $Ag_nPb_mSb_nTe_{m+2n}$ class of materials are in progress, to explore the role of the Ag/Sb distribution and its general dispersing tendencies in the cubic lattice (*21*).

The $Ag_nPb_mSb_nTe_{m+2n}$ materials may find potential applications in thermoelectric power generation from heat sources: for example, vehicle exhaust, coal-burning installations, electric power utilities, etc. With an average *ZT* of 2, a hot source of 900 K, and a temperature difference across 500 K, a conversion efficiency of more than 18% may be achieved (*22*). Additional amplification in *ZT* should be possible with further exploration of doping agents and *n*/*m* values. We have already observed substantially lower thermal conductivities (as much as 40 to 50% lower) in other $Ag_nPb_mSb_nTe_{m+2n}$ members that could further enhance *ZT* values.

References and Notes

1. *ZT* = (σ*S*^{2}/κ)*T*, where σ is the electrical conductivity, *S* is the thermopower or Seebeck coefficient, κ is the thermal conductivity, and *T* is the temperature. The numerator (σ*S*^{2}) is called the power factor.
2. M. G. Kanatzidis, *Semicond. Semimet.* **69**, 51 (2000).
3. C. Uher, *Semicond. Semimet.* **69**, 139 (2000).
4. B. C. Sales, D. Mandrus, R. K. Williams, *Science* **272**, 1325 (1996).
5. S. J. Poon, *Semicond. Semimet.* **70**, 37 (2001).
6. I. Terasaki *et al.*, *Jpn. J. Appl. Phys.* **40**, L65 (2001).
7. B. C. Sales *et al.*, *J. Solid State Chem.* **146**, 528 (1999).
8. G. S. Nolas, G. A Slack, S. B. Schujman, *Semicond. Semimet.* **69**, 255 (2001).
9. S. Latturner *et al.*, *J. Solid State Chem.* **151**, 61 (2000).
10. T. M. Tritt, R. T. Littleton, *Semicond. Semimet.* **70**, 179 (2001).
11. R. Venkatasubramanian *et al.*, *J. Cryst. Growth* **170**, 817 (1997).
12. T. C. Harman, D. L. Spears, M. J. Manfra, *J. Electron Mater.* **25**, 1121 (1996).
13. H. Beyer *et al.*, *Appl. Phys. Lett.* **80**, 1216 (2002).
14. R. Venkatasubramanian *et al.*, *Nature* **413**, 597 (2001).
15. T. C. Harman *et al.*, *Science* **297**, 2229 (2002).

16. D. Y. Chung *et al.*, *Science* **287**, 1024 (2000).
17. Materials and methods are available as supporting material on *Science* Online.
18. D. Y. Chung *et al.*, *Chem. Mater.* **9**, 3060 (1997).
19. These data were obtained with the flash diffusivity–specific heat method at the Thermophysical Properties Research Laboratory, West Lafayette, IN (www.tprl.com/). The sample configuration was in the form of a flat disk of ~14-mm diameter and 2.5-mm thickness.
20. Hall measurements of samples with $m = 18$ and $1 - x = 0.55$ and 0.67 were carried out as a function of temperature. The carrier concentrations (electrons) at room temperature were $\sim 2.15 \times 10^{19}$ and $\sim 1.9 \times 10^{19}$ cm^{-3}, respectively. Carrier concentrations rise sharply with falling temperature, suggesting a narrowing of the band gap in these materials. This is opposite to what occurs in most semiconductors (in which the band gap widens with falling temperature) and similar to what occurs in PbTe (*23*). At the same time, the electron mobilities are markedly high for both $x = 0.55$ and 0.67 samples at ~800 cm^2/V·s and similar to those reported for the MBE-grown thin-film superlattice PbSe/PbTe systems (*15*).
21. D. Bilc *et al.*, in preparation.
22. The power conversion efficiency of a thermoelement is given by

$$\eta = (\Delta T/T_{hot})[(1+ZT_{ave})^{1/2}-1]/[(1+ZT_{ave})^{1/2}+(T_{cold}/T_{hot})]$$

where ΔT is the temperature difference across the device. The first fraction in this expression is the Carnot efficiency. ZT is defined in (*1*).
23. Y. I. Ravich, B. A. Efimova, I. A. Smirnov, *Semiconducting Lead Chalcogenides*, T. S. Stil'bans, Ed. (Plenum, New York, 1970), pp. 323–346.
24. L. Genzel, *Z. Phys.* **135**, 177 (1953).
25. S. Loo, T. Hogan, in preparation.
26. Financial support from the Office of Naval Research and Defense Advanced Research Projects Agency is gratefully acknowledged.

Supporting Online Material

www.sciencemag.org/cgi/content/full/303/5659/818/DC1

Materials and Methods

Fig. S1

27 October 2003; accepted 11 December 2003

Superlattices of Iron Nanocubes Synthesized from $Fe[N(SiMe_3)_2]_2$

Frédéric Dumestre,[1,2] Bruno Chaudret,[1]* Catherine Amiens,[1] Philippe Renaud,[2] Peter Fejes[3]

The reaction of the metal-organic precursor $Fe[N(SiMe_3)_2]_2$ with H_2 in the presence of a long-chain acid and a long-chain amine in various proportions produces monodisperse zerovalent iron nanoparticles. These Fe particles display magnetic properties that match those of bulk iron as evidenced by magnetic and Mössbauer measurements. The nanoparticles adopt a cubic shape with edges of 7 nanometers and are incorporated into extended crystalline superlattices containing nanocubes in close proximity and with their crystallographic axes aligned. These superlattices are formed in solution, precipitate in high yield, and may be redissolved and redeposited as two-dimensional arrays.

The assembly of nanoparticles in electronic devices (*1*) appears as a bottom-up alternative to present lithography techniques for the fabrication of ever smaller devices in microelectronics and for the magnetic-storage industry. For example, magnetic hard drives presently use sensitive read heads formed of thick multilayers of metal nanoparticles (*2*). However, new applications such as single electron devices (*3*) and spin–dependent tunneling (*4*) require a fine-tuning of the physical properties of the nanoparticles and, in turn, a nanometer-scale control of the material, in terms of size, shape, composition, and crystal structure, as well as an organization into two-dimensional (2D) or 3D nanocrystal superlattices.

These devices also require high performance of individual nanoparticles, namely high magnetization and adjustable anisotropy. Recent results have shown that chemical synthetic methods, in particular those based on the use of organometallic precursors, may provide particles displaying magnetic properties similar to gas phase clusters in ultrahigh vacuum (*5*), with control over their shape and hence magnetic anisotropy (*6*, *7*), and that they may be assembled into 2D or 3D superlattices (*8*). However, this does not apply to iron or to iron-based alloys. Chemical syntheses of iron nanoparticles have used $Fe(CO)_5$ as a precursor. For example, upon sonolysis of $Fe(CO)_5$ in the presence of polyvinylpyrrolidone or oleic acid (*9*), amorphous iron nanoparticles are produced in good yields. Similarly, Hyeon has described the synthesis of elongated *bcc* iron particles (*10*) but, in most cases, the magnetization was either found depleted (*9*, *11*) or not reported (*10*). A recent paper, however, describes a high temperature decomposition of $Fe(CO)_5$ in the presence of oleic acid and/or oleylamine leading to nanoparticles of controlled size and magnetization up to 200 A m^2 kg_{Fe}^{-1} (*12*).

Iron-based materials are highly desirable for magnetic applications because of their high magnetization (FeCo, FeNi) and wide range of magnetic anisotropy (FeNi, FePt). Thus, it was of interest to find an easily accessible precursor that would decompose under mild conditions, leave residues that would not perturb the magnetic properties of the resulting particles, and therefore lead to nanoparticles, the size, shape, and surface ligands of which could be controlled. The latter point is of special interest for further assembling the particles into 2D or 3D superlattices. After exploring several organometallic complexes, we considered amido complexes because such compounds have previously been shown to be versatile precursors for the production of particles of industrial interest (*13*) or crystalline 3D superlattices (*14*). We now find that the derivative $Fe[N(SiMe_3)_2]_2$ (where Me ≡ -CH_3) reported by Andersen (*15*) fulfills all requirements.

The decomposition of $Fe[N(SiMe_3)_2]_2$ was carried out in solution at 150°C under a dihydrogen atmosphere in the presence of hexadecylamine (HDA) and a long-chain acid (oleic acid, OA, or hexadecylamonium chloride, HDAC). In a standard reaction, 1 mmol of $Fe[N(SiMe_3)_2]_2$ was dissolved in 20 mL of mesitylene and reacted at 150°C for 48 hours with 3 bar of H_2 (initial pressure at room temperature in the reactor) in the presence of 2 equivalents (eq) of HDA and 1 eq acid. In both cases, a black precipitate forms in ~50% yield, which is shown by transmission electron microscopy (TEM) and scanning electron microscopy (SEM) to consist of iron nanocubes included in extended 3D superlattices (Fig. 1A, Fig. 2, and fig. S1). The superlattices display defined shapes (cubes, parallelograms) with extended faces in the micron range as shown by SEM (Fig. 2B and fig. S1). The nanocubes adopt the *bcc* structure of bulk iron as evidenced by x-ray diffraction (fig. S2) and by a selected area electron diffraction experiment on one of these superlattices; discrete sharp spots are observed that confirm both the *bcc* structure of the nanocubes and the alignment of all their crystallographic axes (Fig. 1B). In the case of the reaction in the presence of OA (HDA:OA; 2:1, **1**), the cube edges display a mean size of 7 nm ($\sigma = 0.4$) and an interparticle spacing estimated at ~1.6 nm, whereas with HDAC (HDA:HDAC; 2:1, **2**), the mean size of the cube edges is measured at 8.3 nm ($\sigma = 0.8$), with an interparticle spacing of ~2 nm. High-resolution electron micrographs (HREM)

[1]Laboratoire de Chimie de Coordination du CNRS, 205, route de Narbonne, 31077 Toulouse Cédex 04, France. [2]Digital DNA Labs, Semiconductor Products Sector, Motorola, le Mirail B.P. 1029, 31023 Toulouse Cedex, France. [3]Digital DNA Labs, Semiconductor Products Sector, Motorola, 2100 East Elliot Road, Tempe, AZ 85824, USA.

*To whom correspondence should be addressed: chaudret@lcc-toulouse.fr